



Revisiting the Full Sets of Orbital Parameters for the XO-3 System: No Evidence for Temporal Variation of the Spin–Orbit Angle

Keduse Worku¹, Songhu Wang², Jennifer Burt³, Malena Rice¹, Xian-Yu Wang^{4,5}, Yong-Hao Wang⁶, Steven S. Vogt⁷, R. Paul Butler⁸, Brett Addison⁹, Brad Holden⁷, Xi-Yan Peng¹⁰, Zhen-Yu Wu^{4,5}, Xu Zhou⁴, Hui-Gen Liu¹¹, Hui Zhang¹⁰, Ji-Lin Zhou¹¹, and Gregory Laughlin¹

¹ Department of Astronomy, Yale University, New Haven, CT 06511, USA

² Department of Astronomy, Indiana University, Bloomington, IN 47405, USA

³ Jet Propulsion Laboratory, California Institute of Technology, 4800 Oak Grove Drive, Pasadena, CA 91109, USA

⁴ National Astronomical Observatories, Chinese Academy of Sciences, Beijing 100012, People’s Republic of China

⁵ University of Chinese Academy of Sciences, Beijing 100049, People’s Republic of China

⁶ School of Physics and Astronomy, Sun Yat-Sen University, Zhuhai 519082, People’s Republic of China

⁷ UCO/Lick Observatory, Department of Astronomy and Astrophysics, University of California at Santa Cruz, Santa Cruz, CA 95064, USA

⁸ Earth and Planets Laboratory, Carnegie Institution for Science, 5241 Broad Branch Road NW, Washington, DC 20015, USA

⁹ University of Southern Queensland, Centre for Astrophysics, USQ Toowoomba, West Street, QLD 4350 Australia

¹⁰ Shanghai Astronomical Observatory, Chinese Academy of Sciences, Shanghai 200030, People’s Republic of China

¹¹ School of Astronomy and Space Science and Key Laboratory of Modern Astronomy and Astrophysics in Ministry of Education, Nanjing University, Nanjing 210093, People’s Republic of China

Received 2019 October 22; revised 2022 January 7; accepted 2022 January 18; published 2022 March 10

Abstract

We present 12 new transit light curves and 16 new out-of-transit radial-velocity measurements for the XO-3 system. By modeling our newly collected measurements together with archival photometric and Doppler velocimetric data, we confirmed the unusual configuration of the XO-3 system, which contains a massive planet ($M_P = 11.92_{-0.63}^{+0.59} M_J$) on a relatively eccentric ($e = 0.2853_{-0.0026}^{+0.0027}$) and short-period (3.19152 ± 0.00145 day) orbit around a massive star ($M_* = 1.219_{-0.095}^{+0.090} M_\odot$). Furthermore, we find no strong evidence for a temporal change of either $V \sin i_*$ (and by extension, the stellar spin vector of XO-3), or the transit profile (and thus orbital angular momentum vector of XO-3b). We conclude that the discrepancy in previous Rossiter–McLaughlin measurements ($70.0^\circ \pm 15.0^\circ$; Hébrard et al. 2008; $37.3^\circ \pm 3.7^\circ$; Winn et al. 2009; $37.3^\circ \pm 3.0^\circ$; Hirano et al. 2011) may have stemmed from systematic noise sources.

Unified Astronomy Thesaurus concepts: [Exoplanets \(498\)](#)

Supporting material: machine-readable table

1. Introduction

The existence of hot Jupiters, giant planets orbiting perilously close to their parent stars, was wholly unpredicted; as a consequence, their initial discoveries 25 years ago occurred with very high signal-to-noise ratio (S/N). In retrospect, this historical development was largely a consequence of the emptiness of the inner reaches of the solar system.

Although it has been suggested that hot Jupiters may form in situ (Batygin et al. 2016), conventional wisdom still holds that they form at larger distances—where cold, ice-based materials are plentiful—and then migrate inward (Bodenheimer et al. 2000). Over the past two decades, two distinct and competing long-distance migration mechanisms have been established: namely, quiescent disk migration (Lin et al. 1996) and violent dynamical migration (Lidov–Kozai cycling with tidal friction, Fabrycky & Tremaine 2007; Wu et al. 2007; Naoz 2016; planet–planet scattering, Rasio & Ford 1996; Nagasawa et al. 2008; or secular interactions, Wu & Lithwick 2011; Petrovich 2015). Nonetheless, the most

workable process for delivering a “normal Jupiter” to its final location remains controversial.

Measurements of stellar obliquity (i.e., the sky-projected angle, λ , between the orbital angular momentum vector of a transiting planet and its host star’s spin vector) through the Rossiter–McLaughlin (R–M) effect (Rossiter 1924; McLaughlin 1924; Queloz et al. 2000) were initially thought to provide a zeroth-order discriminating test between quiescent disk-driven migration and violent dynamical migration. Hot Jupiters with low spin–orbit angles were thought to have migrated through the disk, while those with high spin–orbit angles were believed to owe their orbits to high-eccentricity dynamical migration.

The origin and evolution of spin–orbit misalignment has since been extensively studied (see Winn & Fabrycky 2015 and references therein), however, and the connection between the spin–orbit misalignment and the migration process may be more complicated than was initially thought. These misalignments can either be primordial (chaotic star formation, Bate et al. 2010; Fielding et al. 2015; magnetic star–disk interactions, Lai et al. 2011; Spalding & Batygin 2014; torques from the stellar companions, Batygin 2012), with planets born in tilted disks, or they can be modified later by postmigration evolution (tidal and magnetic realignment, Winn et al. 2010; Dawson 2014; Li & Winn 2016; gravitational perturbation from the companions, Innanen et al. 1997; Li et al. 2014; Storch et al. 2014; Lai 2016; Gomes et al. 2017; internal gravity waves, Rogers et al. 2012). The spin–orbit angle



Original content from this work may be used under the terms of the [Creative Commons Attribution 4.0 licence](#). Any further distribution of this work must maintain attribution to the author(s) and the title of the work, journal citation and DOI.

Table 1
Overview of Observations and Data Reduction for XO-3

Date (UTC)	Time (UTC)	Telescope	Band	Frames	Exposure (s)	Read (s)	Airmass	Moon Illum.	Aperture ^a (pixels)	Scatter ^b (mmag)
2014 Mar 02	10: 43: 00 → 16: 01: 40	Xinglong 60 cm	<i>R</i>	306	60	3	1.06 → 1.88	0.03	18	1.7
2014 Dec 11	12: 05: 58 → 16: 27: 51	Xinglong Schmidt	<i>R</i>	464	20	12	1.21 → 1.05 → 1.07	0.75	16	2.5
2014 Dec 27	11: 15: 39 → 15: 32: 22	Xinglong Schmidt	<i>R</i>	515	18	12	1.18 → 1.05 → 1.08	0.38	17	2.2
2015 Feb 16	10: 37: 34 → 16: 45: 33	Xinglong 60 cm	<i>R</i>	269	60	23	1.05 → 1.82	0.08	30	1.6
2016 Jan 14	10: 15: 34 → 15: 31: 46	Xinglong 60 cm	<i>R</i>	336	10–25	6	1.17 → 1.05 → 1.15	0.25	23	1.7
2016 Feb 02	11: 17: 33 → 15: 47: 20	Xinglong Schmidt	<i>R</i>	460	25	12	1.05 → 1.35	0.35	18	1.5
2016 Feb 15	10: 43: 10 → 13: 28: 28	Xinglong Schmidt	<i>R</i>	198	25–55	12	1.05 → 1.15	0.54	18	2.4
2016 Feb 18	10: 35: 44 → 14: 54: 19	Xinglong 60 cm	<i>R</i>	550	10–25	6	1.05 → 1.38	0.84	18	2.7
2016 Mar 05	11: 33: 32 → 16: 02: 43	Xinglong 60 cm	<i>R</i>	506	25–45	6	1.11 → 2.00	0.15	20	2.2
2017 Nov 11	11: 07: 08 → 14: 59: 15	Xinglong 60 cm	<i>B</i>	97	20–30	23	1.82 → 1.12	0.41	23	4.8
2017 Nov 11	11: 08: 05 → 14: 57: 34	Xinglong 60 cm	<i>V</i>	96	20–30	23	1.82 → 1.12	0.41	23	3.6
2017 Nov 14	15: 31: 09 → 21: 57: 23	Xinglong 60 cm	<i>R</i>	336	20	23	1.08 → 1.05 → 1.55	0.14	25	2.3

Notes.

^a This column indicates the aperture diameter used in SExtractor.

^b This column presents the rms scatter of residuals from the best-fitting model.

generally evolves on very long timescales. Under certain circumstances, however, it can vary on an observable timescale (see, e.g., Rogers et al. 2012).

In this light, the XO-3 system (Johns-Krull et al. 2008) has a special importance as one of few transiting planet systems that displays a discrepancy between multiple R-M measurements ($70^{\circ}0 \pm 15^{\circ}0$, Hébrard et al. 2008; $37^{\circ}3 \pm 3^{\circ}7$, Winn et al. 2009; $37^{\circ}3 \pm 3^{\circ}0$, Hirano et al. 2011). This discrepancy, in combination with the planet’s unusual mass ($M_p = 11.7 M_J$; Bonomo et al. 2017)—lying just at the mass limit between giant planets and low-mass stars—its eccentricity ($e = 0.28$; Wong et al. 2014), and its short period ($P = 3.19$ days; Winn et al. 2008), suggests that XO-3 merits further scrutiny.

In this paper, we present new transit light curves and Doppler velocimetric measurements for XO-3 to address the source of the discrepancy in previous R-M measurements, as well as implications for the origins of hot Jupiters.

The paper is organized as follows. Section 2 presents 33 photometric transit observations from the literature and 12 new transits, as well as 16 new Doppler velocity measurements of XO-3 that were used in this study. Section 3 focuses on the characterization of the stellar atmospheric parameters using the Automated Planet Finder (APF) data. Section 4 describes the joint analysis of the in-transit photometric and out-of-transit radial-velocity measurements. Section 5 compares these findings with previous results and outlines the potential implications of this study.

2. Observation and Data Reduction

2.1. Photometry

Our new photometric data set, composed of 12 light curves, was collected using the Xinglong Schmidt and Xinglong 60 cm telescopes operated by the National Astronomical Observatories of China. These observations span roughly 4 yr, from 2014 March to 2017 December.

Four of these light curves were obtained using the Xinglong Schmidt telescope (Zhou et al. 1999, 2001), which utilizes a $4K \times 4K$ CCD. This CCD has a field of view (FOV) of $94' \times 94'$ and a pixel scale of $1''.38 \text{ pixel}^{-1}$. To reduce the initial readout time (93 s), we windowed the frames down to 512×512 pixels, which results in a readout time of 12 s. A

Johnson/Cousins *R*-band filter was used during these observations.

The remaining eight light curves were obtained with the Xinglong 60 cm telescope. The observation conducted on UT 2014 March 2 used a 512×512 CCD, giving an FOV of $17' \times 17'$, a pixel scale of $1''.95 \text{ pixel}^{-1}$, and a readout time of 3 s. The observations conducted on UT 2015 February 16, UT 2017 November 11, and UT 2017 November 14 used a $1K \times 1K$ CCD, giving an FOV of $17' \times 17'$, a pixel scale of $0''.99 \text{ pixel}^{-1}$, and a readout time of 23 s. The observations conducted on UT 2016 January 14, UT 2016 February 18, and UT 2016 March 5 used a $2K \times 2K$ CCD, giving an FOV of $36' \times 36'$, a pixel scale of $1''.06 \text{ pixel}^{-1}$, and a readout time of 6 s. All of the observations for this telescope utilized a Johnson/Cousins *R*-band filter, except the one from UT 2017 November 11, which alternated between the Johnson/Cousins *B*-band and *V*-band filters.

As XO-3 is bright ($V_{\text{mag}} = 9.86$), we defocused the telescopes to avoid nonlinear effects on the CCD. The defocusing method usually requires longer exposure times, which is helpful for increasing the duty cycle of our observations and reducing the scintillation and Poisson noise (Southworth et al. 2009). The focus was kept unchanged during our observation. The exposure time was changed only if required by weather conditions. The telescope time was synchronized with online GPS time servers. The beginning time of each exposure was recorded in the frame header using the UTC time standard, and it was then converted to BJD_{TDB} as described in Eastman et al. (2010). All times reported from previous works have been converted to BJD_{TDB} for congruency with our time standard.

We conducted standard bias and flat-field corrections on all the frames following the procedures described in Wang et al. (2017, 2018, 2018a, 2018c, 2019, 2021a). We then performed aperture photometry using SExtractor (Bertin & Arnouts 1996). We identified the best aperture for both the target and reference stars as the one that minimized the rms of the final differential light curves, which are obtained by comparing XO-3 with three reference stars in the field. Highly discrepant points and/or linear trends presented in these light curves were removed. A summary of the observations and the data reduction procedures

Table 2
Photometry for XO-3

BJD	Flux	σ_{Flux}	Instrument	Filter
2,456,719.055590	0.9950	0.0017	Xinglong 60 cm	R
2,456,719.056318	0.9943	0.0017	Xinglong 60 cm	R
2,456,719.057046	0.9948	0.0017	Xinglong 60 cm	R
2,456,719.057773	0.9965	0.0017	Xinglong 60 cm	R
2,456,719.058501	0.9956	0.0017	Xinglong 60 cm	R
2,456,719.059229	0.9940	0.0017	Xinglong 60 cm	R
2,456,719.059957	0.9947	0.0017	Xinglong 60 cm	R
2,456,719.060685	0.9935	0.0017	Xinglong 60 cm	R
2,456,719.061412	0.9962	0.0017	Xinglong 60 cm	R
2,456,719.062140	0.9943	0.0017	Xinglong 60 cm	R
2,456,719.062868	0.9944	0.0017	Xinglong 60 cm	R
2,456,719.063597	0.9935	0.0017	Xinglong 60 cm	R
...

(This table is available in its entirety in machine-readable form.)

are listed in Table 1. The final light curves are presented in Table 2 and plotted in Figures 1 and 2.

2.2. Velocimetry

XO-3 has been the subject of a variety of radial-velocity (RV) observing campaigns over the past two decades. In this work, we combine all previously published RV data sets with a new set of velocity measurements obtained using the APF telescope located at Lick Observatory. The APF couples a 2.4 m primary mirror with the slit-fed, Levy echelle spectrograph, which works at a typical spectral resolution of $R \sim 110,000$ and delivers a peak overall system efficiency (fraction of photons striking the telescope primary that are detected by the CCD) of 15% (Vogt et al. 2014). The telescope was designed to search for planets in the liquid water habitable zone of nearby stars. The APF is driven by a dynamic scheduling software system that can make minute-to-minute decisions on what target to observe based on the ambient atmospheric transparency, atmospheric seeing, and lunar phase (Burt et al. 2015). This allows the telescope to operate efficiently throughout the year without the need for human supervision.

Like its predecessors on the Keck and Magellan telescopes (HIRES: Vogt et al. 1994, and PFS: Crane et al. 2010, respectively), the APF uses a gaseous I_2 cell to imprint a forest of narrow absorption lines on the stellar spectrum before its incidence on the spectrograph slit (Butler et al. 1996). These I_2 absorption lines create a stable wavelength calibration source and permit the measurement of the spectrometer’s point-spread function (PSF). For each stellar spectrum, the 5000–6200 Å region (which contains the highest density of I_2 lines) is subdivided into ~ 700 individual 2 Å segments, with each segment providing an independent measure of the wavelength, the PSF, and the Doppler shift. Our reported overall stellar velocity from a given spectrum is a weighted mean of the individual segments’ velocity measurements. The uncertainty for each velocity is the rms of the individual segment velocity values about the mean divided by the square root of the number of segments. This “internal” uncertainty primarily represents errors in the fitting process, which are dominated by Poisson statistics. The velocities are expressed relative to the solar system barycenter, but are not referenced to any absolute fiducial point. Since it began scientific operations in Q2 2013,

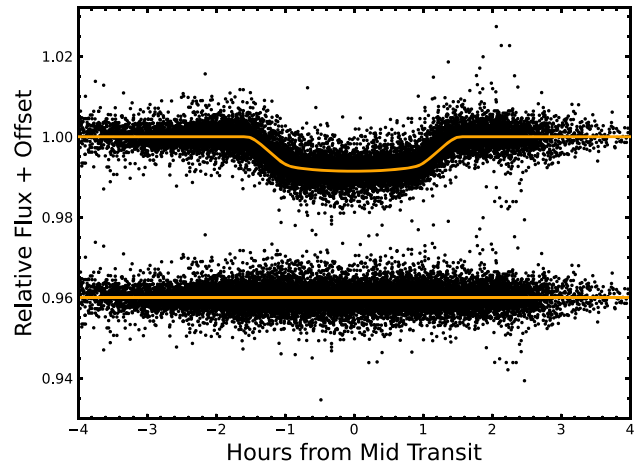


Figure 1. Phased light curve of XO-3b including 33 literature transits provided by previous works (Johns-Krull et al. 2008; Winn et al. 2008, 2009; Bonomo et al. 2017) and 12 new transits collected in this work. To estimate the system parameters, these light curves were simultaneously fitted with the radial-velocity measurements (Figure 3) as described in detail in Section 4. The orange solid line represents the best-fitting model to all of the data, and the residuals are plotted below.

the APF has contributed to a number of planet detections (e.g., Burt et al. 2014, 2021; Fulton et al. 2015; Vogt et al. 2015; Christiansen et al. 2017) and has showcased its ability to reach internal precisions of $\sim 1 \text{ m s}^{-1}$ on bright, quiet stars. Indeed, the APF has consistently achieved internal velocity precision of order $\sigma \lesssim 2 \text{ m s}^{-1}$ on bright (e.g., $V \lesssim 8$) stars (Vogt et al. 2015).

Table 3 presents our newly collected RV measurements for XO-3b, with 16 individual exposures. The median internal uncertainty for our observations is $\sigma_i \approx 15.9 \text{ m s}^{-1}$ with an exposure time of 45 minutes. These large internal uncertainties are driven by (1) the star’s high rotational velocity ($V \sin i_* = 17.3 \pm 0.9 \text{ km s}^{-1}$; see Section 3 for more details), which rotationally broadens the stellar absorption lines, thereby reducing their Doppler information content, and (2) by the star’s high effective temperature ($T_{\text{eff}} = 6471^{+83}_{-82} \text{ K}$), which reduces the overall number of absorption lines (Bouchy et al. 2011; Torres et al. 2012; Beatty & Gaudi 2015).

These APF velocities are combined with previously published RV data sets from the following instruments (Figure 3): the High Resolution Echelle Spectrometer (HIRES) on Keck I (Vogt et al. 2014), the northern High Accuracy Radial velocity Planet Searcher (HARPS-N) on the Telescopio Nazionale Galileo (Cosentino et al. 2012, 2014), the Spectrographe pour l’Observation des Phénomènes des Intérieurs stellaires et des Exoplanètes (SOPHIE) on the 1.93 m reflector telescope at the Haute-Provence Observatory (Perruchot et al. 2008), the High Dispersion Spectrograph (HDS) on the Subaru telescope (Noguchi et al. 2002), the High Resolution Spectrograph (HRS) on the Hobby-Eberly Telescope and the Tull Coude spectrograph on the HJS telescope (though, in this case, it was coupled to the Hobby-Eberly Telescope via a fiber optic cable; Tull et al. 1995; Tull 1998), and the eShel spectrograph at Stara Lesna Observatory (SLO; Eversberg 2016). Detailed information on each RV data set can be found in the reference list in Table 4.

Like the APF and Keck/HIRES, HET’s HRS makes use of an iodine cell for its wavelength calibration efforts and applies

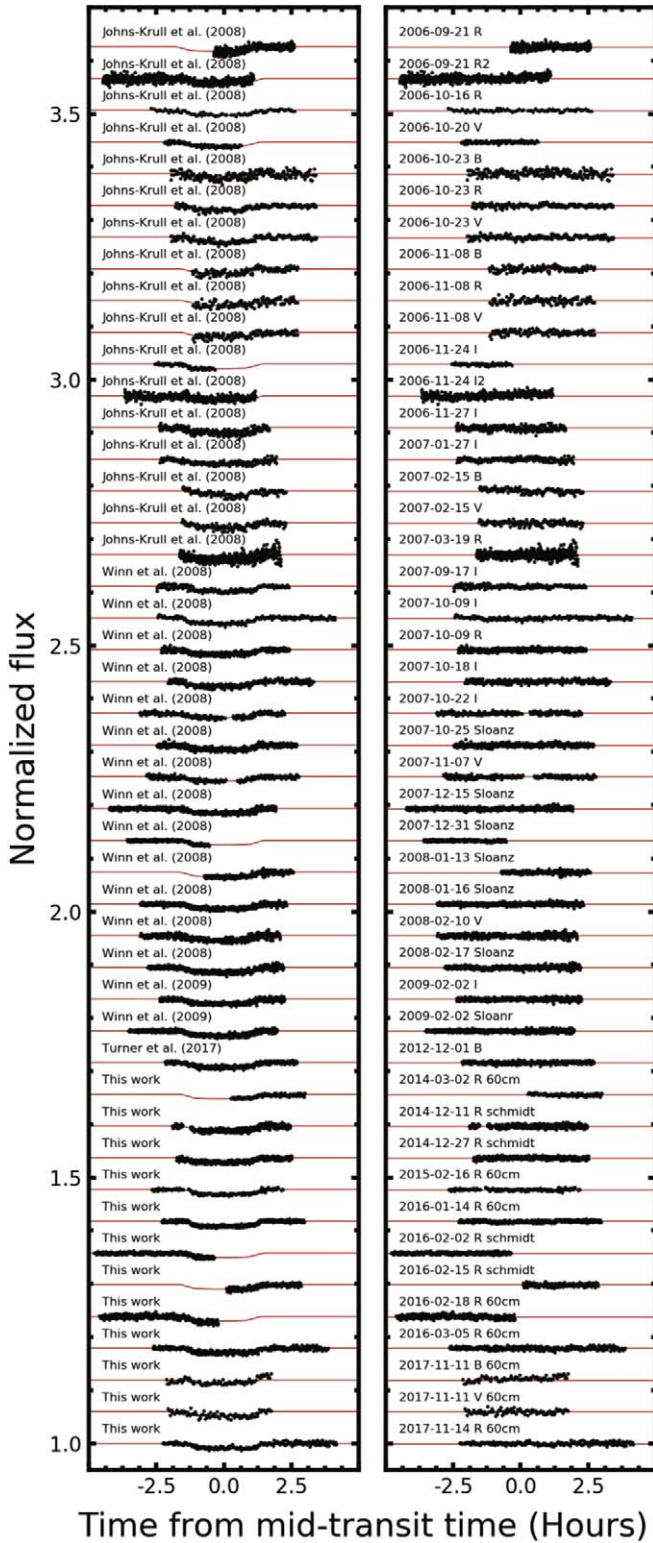


Figure 2. Light curves of XO-3b transits, obtained from the literature and as part of this work. The best-fitting models are overplotted as solid red lines in the left panel. The residuals are displayed in the right panel. Both light curves and residuals are sorted by observation date for clarity.

a forward-modeling approach for determining each observation’s RV measurement. The other instruments listed here handle wavelength calibration with reference spectra taken using a ThAr calibration lamp, either via simultaneous

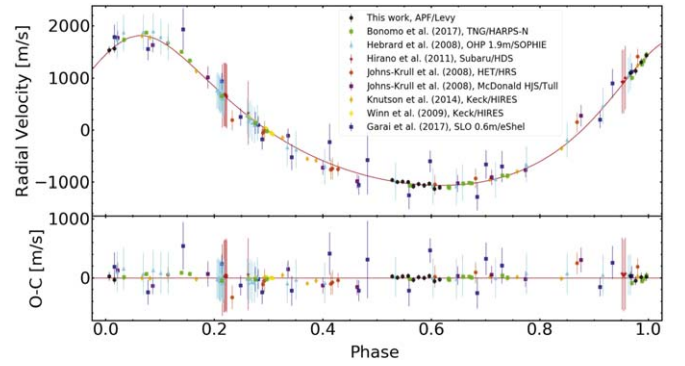


Figure 3. The radial-velocity measurements of XO-3 from previous works (Hirano et al. 2011; Hébrard et al. 2008; Johns-Krull et al. 2008; Winn et al. 2009; Knutson et al. 2014; Bonomo et al. 2017; Garai et al. 2017) and from this work, marked as different colors and shown as a function of orbital phase. The best-fitting Keplerian orbit model (solid red line) is determined from the joint fitting of RVs and light curves. The residuals of the best fit, with an rms scatter $\sigma = 267.90 \text{ m s}^{-1}$, are shown in the bottom panel.

Table 3
APF RVs for XO-3

BJD	RV (m s^{-1})	σ_{RV} (m s^{-1})
2,457,683.767	-918.53333	14.410
2,457,683.798	-951.22600	15.857
2,457,683.830	-946.57400	15.773
2,457,683.861	-951.54200	14.680
2,457,683.892	-1031.46600	15.292
2,457,683.923	-994.45200	14.566
2,457,683.955	-1016.47200	15.046
2,457,683.986	-986.96500	14.303
2,457,684.017	-1077.11600	15.232
2,457,684.048	-1050.91000	16.088
2,457,809.638	383.11333	25.398
2,457,809.669	422.80429	23.685
2,457,809.700	596.86000	23.145
2,457,809.732	720.67714	18.881
2,457,809.763	824.05000	18.534
2,457,809.794	852.69000	22.612

reference spectra in the case of fiber-fed instruments or via separate calibration frames for the slit-fed instruments.

For the instruments with a ThAr-based wavelength calibration, a 2D spectrum is extracted from the FITS file once an observation is complete. The stellar spectrum is cross-correlated with a reference (in the case of HARPS-N, SOPHIE, and HDS this is a numerical mask corresponding to the appropriate spectral type, while for the Tull Coude spectrograph it is a particular spectrum of XO-3 taken on BJD 2,454,137.8215). The resulting cross-correlation function (CCF) is fit with a Gaussian curve to produce a radial-velocity measurement, and it is calibrated to determine the RV photon-noise uncertainty σ_{RV} (e.g., Baranne et al. 1996; Pepe et al. 2002).

3. Stellar Atmospheric Parameters from APF

We determined the values of the stellar atmospheric parameters, including $V \sin i_*$, T_{eff} , and $\log g$, for XO-3 directly from our APF spectrum using The Cannon (Ness et al. 2015; Casey et al. 2016), a data-driven approach using

Table 4
RV Data Sources

Reference	Facility	Calibration	N_{obs}	rms (m s^{-1})
This work	Levy (APF)	I ₂ cell	16	29.95
Bonomo et al. (2017)	HARPS-N (TNG)	ThAr lamp	19	44.13
Hébrard et al. (2008)	SOPHIE (1.93 m, HPO)	ThAr lamp	34	66.37
Hirano et al. (2011)	HDS (Subaru)	ThAr lamp	10	47.64
Johns-Krull et al. (2008)	HRS (HET)	I ₂ cell	11	151.41
Johns-Krull et al. (2008)	Tull Coude (HJS)	I ₂ cell	10	141.73
Knutson et al. (2014)	HIRES (Keck I)	I ₂ cell	11	37.20
Winn et al. (2009)	HIRES (Keck I)	ThAr lamp	11	11.45
Garai et al. (2017)	eShel (0.6 m, SLO)	ThAr lamp	20	269.30

Table 5
Stellar Parameters for XO-3

Telescope	HJS	Keck	Keck	Subaru	Subaru+Keck	Keck+TRES	APF
Instrument	Tull Coude	HIRES	HIRES	HDS	HDS+HIRES	HIRES+FIES	Levy
Observation Date	2006 Oct–2007 Feb	2009 Feb	2009 Feb	2009 Nov–2010 Feb	2009 Feb–2010 Feb	2009 Feb	2016 Oct
Method	SME	SME	R-M Fitting	R-M Fitting	R-M Fitting	SPC+SME+MOOG	Cannon
References	1	2	3	4	4	5	This Work
T_{eff} (K)	6429 ± 50	6673 ± 25	6759 ± 79	6430 ± 69
[M/H]	-0.204 ± 0.023	-0.054 ± 0.01	-0.05 ± 0.08	...
$\log g$ (cm s^{-2})	3.95 ± 0.062	4.15 ± 0.028	$4.24 \pm 0.03^{\text{a}}$	4.3 ± 0.1
$V \sin i_*$ (km s^{-1})	18.54 ± 0.17	16.19 ± 0.5	18.31 ± 1.3	17.0 ± 1.2	18.4 ± 0.8	20.3 ± 2.0	17.3 ± 0.9

Note.

^a External constraint on $\log g$ was obtained from the light curves (Winn et al. 2008).

References: (1) Johns-Krull et al. (2008); (2) Brewer et al. (2016); (3) Winn et al. (2009); (4) Hirano et al. (2011); (5) Torres et al. (2012).

generative modeling to determine stellar parameters. The Cannon trains on an input set of stellar spectra with previously determined parameter values in order to “learn” the characteristics of this data set. This trained model can then be applied to obtain the corresponding labels for a new set of input spectra. The Cannon requires overlapping wavelength coverage and assumes a similar set of systematics between the training set of spectra and the data to which it is applied.

Following the methods of Rice & Brewer (2020), we ran The Cannon to determine the properties of XO-3 directly from our APF spectrum. We trained our model using Keck/HIRES spectra included in the Spectral Properties of Cool Stars (SPOCS) data set (Valenti & Fischer 2005; Brewer et al. 2016), with stellar parameters determined using the program Spectroscopy Made Easy (SME; Valenti & Piskunov 1996).

From the full SPOCS sample, we removed all spectra flagged as “bad” or labeled with “NGC,” indicating that the target was not an individual star. We also cut all spectra from our input sample with $S/N < 100$, and we used only the highest- S/N spectrum for each star in the sample. This resulted in a total of 1202 spectra in our training/validation sample. We used 86 overlap stars observed by both Keck/HIRES (as part of the SPOCS sample) and by the APF as a validation set to test our model performance, leaving 1116 stars in our training sample.

We interpolated the HIRES and APF spectra onto an overlapping wavelength grid to directly compare each spectrum. Then, we trained our model using only HIRES spectra and applied it to our overlapping validation set of APF spectra to determine uncertainties in each parameter. Our final values for XO-3 are included in Table 5.

Because we trained our model using HIRES spectra, the differing systematics between the Keck and APF instrumentation setups may affect the precision of our label transfer process. Indeed, we find that the scatter when transferring labels across data sets, quantified using our validation set, is higher than when using only Keck/HIRES spectra as in Rice & Brewer (2020). This results in higher uncertainties for our reported values. From our validation set, we also find a systematic offset in the values of $V \sin i_*$ derived from our APF spectra relative to the nominal SPOCS values; that is, the $V \sin i_*$ values obtained for APF spectra with The Cannon are on average -1.87 km s^{-1} lower than the associated SPOCS values. This offset is likely attributable to the difference in the line-spread function of the APF as compared to that of Keck/HIRES. We correct for this offset in Table 5.

XO-3 is also included in the SPOCS sample with previously determined stellar parameters obtained based on the Keck spectra alone. We compared these preexisting parameters with our results as an additional test to check the fidelity of our model, focusing on $\log g$ and T_{eff} , two other dominant global stellar properties that should show no temporal changes. As shown in Table 5, we find that all global stellar parameters obtained for XO-3 from the APF data are in agreement with previously reported values derived from the HIRES data set.

Our results are detailed in Table 5. We report our uncertainties as the scatter in our test set results when testing and training with the SPOCS sample; these uncertainties may be underestimated due to the differing systematics across instruments, which are not encompassed by this scatter. Although our stellar atmospheric parameters from APF data show good agreement with previous estimates derived from a

Table 6
System Parameters for XO-3

Parameter	Units	This Work	Previous Work	Agreement(σ)	Ref.
Stellar Parameters:					
M_*	Mass (M_\odot)	$1.219^{+0.090}_{-0.095}$	1.213 ± 0.066	0.05	Winn2008
R_*	Radius (R_\odot)	$1.371^{+0.041}_{-0.042}$	1.377 ± 0.083	0.06	Winn2008
L_*	Luminosity (L_\odot)	$2.97^{+0.27}_{-0.26}$	$2.92^{+0.59}_{-0.48}$	0.09	Winn2008
ρ_*	Density (cgs)	$0.665^{+0.033}_{-0.030}$	0.650 ± 0.086	0.16	Winn2008
$\log g$	Surface gravity (cgs)	$4.249^{+0.017}_{-0.018}$	4.244 ± 0.041	0.11	Winn2008
T_{eff}	Effective temperature (K)	6471^{+83}_{-82}	6429 ± 100	0.32	Winn2008
[Fe/H]	Metallicity	$-0.176^{+0.080}_{-0.081}$	-0.177 ± 0.080	0.01	Winn2008
[Fe/H] ₀	Initial metallicity	$-0.025^{+0.072}_{-0.071}$
Age	Age (Gyr)	$2.6^{+1.6}_{-1.1}$	$2.82^{+0.58}_{-0.82}$	0.18	Winn2008
EEP	Equal evolutionary point	361^{+39}_{-21}
A_V	V-band extinction	$0.069^{+0.091}_{-0.049}$
σ_{SED}	SED photometry error scaling	$2.8^{+2.8}_{-1.1}$
d	Distance (pc)	$178.6^{+6.9}_{-7.4}$	174 ± 18	0.24	Winn2008
π	Parallax (mas)	$5.60^{+0.24}_{-0.21}$
Planetary Parameters:					
P	Period (days)	3.19152 ± 0.00145^a	3.1915239 ± 0.0000068	0.00	Winn2008
R_P	Radius (R_J)	$1.219^{+0.039}_{-0.040}$
T_C	Time of transit (BJD _{TDB})	$2454449.86969 \pm 0.00073^a$	$2454449.868937 \pm 0.00023$	0.99	Winn2008
T_0	Optimal transit time (BJD _{TDB})	$2455314.77290 \pm 0.00015$
a	Semimajor axis (au)	$0.0455^{+0.0011}_{-0.0012}$	$0.04539^{+0.00081}_{-0.00084}$	0.08	Bonomo2017
i	Inclination (deg)	84.26 ± 0.19	84.20 ± 0.54	0.1	win2008
e	Eccentricity	$0.2853^{+0.0027}_{-0.0026}$	$0.27587^{+0.00071}_{-0.00067}$	3.39	Bonomo2017
ω_*	Argument of periastron (deg)	349.6 ± 1.2	$349.35^{+0.67}_{-0.68}$	1.78	Bonomo2017
T_{eq}	Equilibrium temperature (K)	1714 ± 26	1710 ± 46	0.08	Winn2008
M_P	Mass (M_J)	$11.92^{+0.59}_{-0.63}$	$11.7^{+0.43}_{-0.43}$	0.3	Bonomo2017
K	RV semi-amplitude (m s^{-1})	$1488.0^{+8.7}_{-9.1}$	$1468.9^{+4.6}_{-4.5}$	1.95	Bonomo2017
$\log K$	Log of RV semi-amplitude	$3.1726^{+0.0025}_{-0.0026}$
R_P/R_*	Radius of planet in stellar radii	$0.09139^{+0.00039}_{-0.00040}$	0.09057 ± 0.00057	1.19	Winn2008
a/R_*	Semimajor axis in stellar radii	$7.12^{+0.12}_{-0.11}$	7.07 ± 0.31	0.15	Winn2008
δ	Transit depth (fraction)	$0.008352^{+0.000071}_{-0.000072}$
Depth	Flux decrement at midtransit	$0.008352^{+0.000071}_{-0.000072}$
τ	Ingress/egress transit duration (days)	0.01904 ± 0.00067	0.466 ± 0.033	0.25	Winn2008
T_{14}	Total transit duration (days)	0.12334 ± 0.00060
T_{FWHM}	FWHM transit duration (days)	0.10430 ± 0.00033
b	Transit impact parameter	$0.700^{+0.011}_{-0.012}$	0.705 ± 0.023	0.19	Winn2008
b_S	Eclipse impact parameter	$0.614^{+0.012}_{-0.013}$
τ_S	Ingress/egress eclipse duration (days)	$0.01509^{+0.00053}_{-0.00052}$
$T_{S,14}$	Total eclipse duration (days)	0.1167 ± 0.0012
$T_{S,\text{FWHM}}$	FWHM eclipse duration (days)	$0.10159^{+0.00069}_{-0.00075}$
$\delta_{S,3.6\mu\text{m}}$	Blackbody eclipse depth at $3.6 \mu\text{m}$ (ppm)	754^{+24}_{-25}
$\delta_{S,4.5\mu\text{m}}$	Blackbody eclipse depth at $4.5 \mu\text{m}$ (ppm)	975 ± 27
ρ_P	Density (cgs)	$8.15^{+0.54}_{-0.50}$	$8.1^{+1.6}_{-1.3}$	0.04	Bonomo2017
$\log g_P$	Surface gravity	$4.298^{+0.017}_{-0.016}$	$4.293^{+0.055}_{-0.053}$	0.09	Bonomo2017
Θ	Safronov number	$0.729^{+0.025}_{-0.023}$
$\langle F \rangle$	Incident flux ($10^9 \text{ erg s}^{-1} \text{ cm}^{-2}$)	1.81 ± 0.11
T_P	Time of periastron (BJD _{TDB})	$2454449.2483^{+0.0086}_{-0.0089}$
T_S	Time of eclipse (BJD _{TDB})	$2454448.8324^{+0.0036}_{-0.0038}$
T_A	Time of ascending node (BJD _{TDB})	$2454449.3105^{+0.0035}_{-0.0037}$
T_D	Time of descending node (BJD _{TDB})	2454447.852 ± 0.010
$e \cos \omega_*$...	$0.2778^{+0.0018}_{-0.0019}$	$0.27111^{+0.00034}_{-0.00033}$	3.65	Bonomo2017
$e \sin \omega_*$...	$-0.0648^{+0.0061}_{-0.0063}$	$-0.0510^{+0.0033}_{-0.0034}$	1.93	Bonomo2017
$M_P \sin i$	Minimum mass (M_J)	$11.86^{+0.58}_{-0.63}$
M_P/M_*	Mass ratio	$0.00934^{+0.00026}_{-0.00023}$	0.00927 ± 0.00036	0.16	Winn2008
d/R_*	Separation at midtransit	7.00 ± 0.13
P_T	A priori nongrazing transit prob	$0.1298^{+0.0023}_{-0.0024}$
$P_{T,G}$	A priori transit prob	0.1559 ± 0.0029
P_S	A priori nongrazing eclipse prob	$0.1478^{+0.0021}_{-0.0022}$
$P_{S,G}$	A priori eclipse prob	0.1776 ± 0.0027

Table 6
(Continued)

Parameter	Units	This Work	Previous Work	Agreement(σ)	Ref.
Wavelength Parameters:					
u_{1B}	Linear limb-darkening coeff	0.497 ± 0.028
u_{2B}	Quadratic limb-darkening coeff	0.277 ± 0.026
u_{1I}	Linear limb-darkening coeff	0.197 ± 0.017	0.06 ± 0.15	0.91	Winn2008
u_{2I}	Quadratic limb-darkening coeff	0.301 ± 0.016	0.35^b	...	Winn2008
u_{1R}	Linear limb-darkening coeff	$0.260^{+0.013}_{-0.014}$	0.16 ± 0.14	0.71	Winn2008
u_{2R}	Quadratic limb-darkening coeff	0.317 ± 0.012	0.37^b	...	Winn2008
$u_{1Sloanr}$	Linear limb-darkening coeff	0.293 ± 0.044
$u_{2Sloanr}$	Quadratic limb-darkening coeff	$0.336^{+0.046}_{-0.045}$
$u_{1Sloanz}$	Linear limb-darkening coeff	0.174 ± 0.019	0.11 ± 0.07	0.88	Winn2008
$u_{2Sloanz}$	Quadratic limb-darkening coeff	0.301 ± 0.019	0.353^b	...	Winn2008
u_{1V}	Linear limb-darkening coeff	$0.366^{+0.020}_{-0.019}$	0.47 ± 0.14	0.74	Winn2008
u_{2V}	Quadratic limb-darkening coeff	0.327 ± 0.019	0.36^b	...	Winn2008

Notes.^a Conservative values from JKTEBOP fit.^b In the fit of Winn et al. (2008), the quadratic coefficient is fixed.

wide range of independent data sets, we adopt $\log g$ and T_{eff} from Torres et al. (2012) as priors in our global fitting (see Section 4 for details) because their parameters benefit from using combined high-S/N data from both Keck/HIRES and TRES/FIES.

Our primary parameter of interest is $V \sin i_*$ (see Section 5 for details), which we compare with previous estimates in Table 5. Ultimately, we find that the value of $V \sin i_*$ that we obtain directly from the APF spectrum is consistent with previous estimates derived from a wide range of independent data sets.

4. Planetary Parameters from Global Fitting

System Parameters. To determine the XO-3 system parameters, we used EXOFASTv2 (Eastman et al. 2013; Eastman 2017) to simultaneously fit the transit light curves and out-of-transit radial-velocity data from the literature (Hébrard et al. 2008; Johns-Krull et al. 2008; Winn et al. 2008, 2009; Hirano et al. 2011; Knutson et al. 2014; Bonomo et al. 2017; Garai et al. 2017), as well as our newly collected photometric and RV data.

EXOFASTv2 performs a global analysis of exoplanetary and stellar parameters using a differential evolution Markov Chain Monte Carlo (DE-MCMC; ter Braak 2006) simulation to simultaneously fit, for an arbitrary number of planets, the spectral energy distribution (SED), transit data, and RV data taken from multiple instruments.

To constrain the stellar parameters, we used the MESA Isochrones and Stellar Tracks (MIST) model (Choi et al. 2016; Dotter 2016) included in EXOFASTv2. The Gaussian priors were applied to the T_{eff} and $[\text{Fe}/\text{H}]$ of the star derived in Torres et al. (2012). The limb-darkening coefficients were assumed to be a quadratic function. We imposed wavelength-dependent priors on limb-darkening coefficients from Claret & Bloemen (2011) based on the T_{eff} , $\log g$, and $[\text{Fe}/\text{H}]$ from Torres et al. (2012). The priors for the orbital parameters, including all transit and RV parameters, were adopted from the results of Winn et al. (2009).

To minimize the convergence time, the fitting process required multiple short runs before longer ones. We derived a new set of Gaussian priors after each run, allowing us to begin

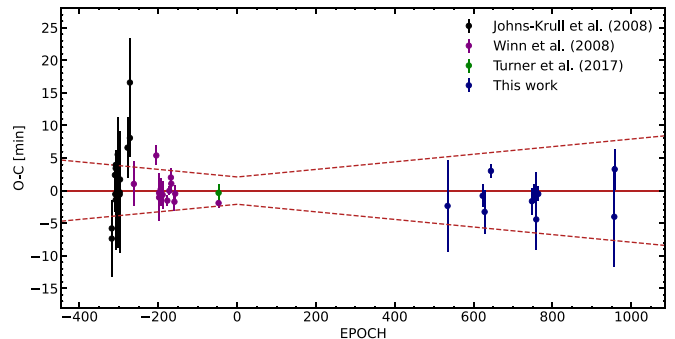


Figure 4. Observed minus calculated midtransit times ($O - C$) for XO-3b, according to the updated linear ephemeris. The $(O - C) = 0$ reference is represented by a red solid line, and the red dashed line indicates the propagation of $\pm 1\sigma$ errors of the updated linear ephemeris.

subsequent fits at the most likely model. We continually refined the fit until our criteria—both the number of independent draws being greater than 1000 and a Gelman–Rubin statistic of less than 1.01 for all parameters—were satisfied six consecutive times, indicating that the chains were considered to be well mixed (Eastman et al. 2013).

The system parameters derived from global fit are listed in Table 6. The fitting results are shown in Figures 1, 2, and 3.

Transit Timing Variations and Orbital Ephemeris. We modeled each available transit light curve for XO-3 using the JKTEBOP (Southworth 2008) code. We fixed all global parameters to the results derived from the global fitting, and we allowed only the transit midtime (T_0) and baseline flux (F_0) to vary as free parameters in the fit. We utilized the bootstrapping technique, Monte Carlo simulations, and the residual-shift method to estimate the errors of midtransit times separately. The largest errors were selected as the final errors to provide a conservative estimate. The result is shown in Figure 4, which is consistent with a constant period. No significant transit timing variations were detected.

To update the linear ephemeris ($T_C + N \times P$), we performed a weighted least-squares fit to the derived midtransit times (T_0). During the fit, we followed the approaches described in Southworth et al. (2017), and we rescaled the uncertainties of each transit midtime such that $\chi_{\text{reduced}}^2 = 1$. This choice was

made to provide conservative errors for the transit midtime at the reference epoch (T_C) and orbital period (P) for future scheduling purposes. The result agrees with the values from Winn et al. (2008) within 1σ .

5. Discussion

Our global analysis of 45 transit light curves (including 12 collected in this work) and 142 Doppler velocities (including 16 collected in this work) spans more than 10 yr, making XO-3b one of the best-studied exoplanets.

The results from our global analysis (Table 6) show good agreement with previous work (Winn et al. 2009; Wong et al. 2014; Bonomo et al. 2017), except that we find a slightly higher eccentricity (e) by 0.01.

Our result confirms that the XO-3 system is unique, containing a massive planet ($M_p = 11.92_{-0.63}^{+0.59} M_J$) in a relatively eccentric ($e = 0.2853_{-0.0026}^{+0.0027}$) and short-period (3.19152 ± 0.00145 day) orbit around a massive star ($M_* = 1.219_{-0.095}^{+0.090} M_\odot$).

Our result also confirms the relatively high Safronov number, $\Theta = 0.73$, of XO-3b (Safronov 1972). The Safronov number is defined as

$$\Theta = \frac{1}{2} \left[\frac{V_{\text{esc}}}{V_{\text{orb}}} \right]^2 = \frac{M_p}{M_*} \frac{a}{R_p}, \quad (1)$$

where $V_{\text{esc}} = \sqrt{2GM_p/R_p}$ is the planetary escape velocity, and $V_{\text{orb}} = \sqrt{GM_*/a}$ is the planet's circular orbital velocity. Θ connects to the outcome of instability in an N -body system (for example, a system that hosts a hot Jupiter and close-in test particles). If $\Theta \gg 1$, the ejection of test particles is very likely when instability occurs, whereas for most hot Jupiters, Θ is substantially smaller than 1, and collisions (either between test particles and the planet, or between test particles and the star) constitute a more likely outcome. Although XO-3b is on a 3 day orbit, its high mass drives its Safronov number close to unity.

We explored the dynamical behavior of test particles on both interior and exterior orbits between 1.3 to 7.5 mutual Hill radii (Gladman 1993) with XO-3b. As shown in Figure 5, the stability of test particles increases with increasing distance from XO-3b. All of the unstable particles initially lay within 3.5 mutual Hill radii of the planet, in concordance with the rule of thumb found by Chambers et al. (1996). In terms of the channels for instability, 80% collided with XO-3, while 20% were ejected from system. The integrations indicate that XO-3 is approaching (but has not reached) a regime in which small bodies in the vicinity of the planet are predominantly ejected from the system rather than incorporated into the planet. This suggests the existence of a crossover mass slightly above that of XO-3 where further growth in mass would be restricted, and it is consistent with the observed near absence of such objects in the short-period planet population (Marcy & Butler 2000), despite their ready detectability through either transit photometry or Doppler velocity.

XO-3b is also known as the first exoplanet measured to have a large spin-orbit misalignment ($70^\circ 0 \pm 15^\circ 0$; Hébrard et al. 2008). Follow-up studies on the stellar obliquity of the XO-3 system based on radial velocities collected with Keck/HIRES and Subaru/HDS found a smaller angle ($37^\circ 3 \pm 3^\circ 7$, Winn et al. 2009; $37^\circ 3 \pm 3^\circ 0$, Hirano et al. 2011). Although there are

indications of systematic effects in previous data sets (see Hirano et al. 2011 for a detailed discussion), the discrepancy could also be caused by true astrophysical reasons that warrant investigation.

Astrophysical Origin. The true angle between the orbital angular momentum vector of XO-3b and its stellar spin vector can be determined from three independent angles: the sky-projected spin-orbit angle (λ), which can be measured through the Rossiter–McLaughlin effect; the orbital angular momentum vector of the transiting planet along the line of sight (e.g., transit inclination, i), which can be determined by modeling the transit light curve; and the stellar spin vector of the star along the line of sight (i_*), which can be estimated by measuring $V_* \sin i_*$ from spectroscopic observation and V_* by analyzing periodic photometric variations in the light curve caused by the stellar spots.

If the discrepancy between previous λ measurements is truly caused by a change in the spin-orbit angle of XO-3 system, then it is statistically improbable that it only changed within the projected plane (perpendicular to the line of sight, e.g., λ). In the following analyses, we examine whether the stellar spin vector of XO-3 along the line of sight (i_*) or the orbital angular momentum vector of XO-3b along the line of sight (e.g., transit inclination, i) also changed over time. We do not find strong evidence in support of these changes.

Stellar Spin Vector along the Line of Sight (i_).* Internal gravity waves within hot (and thus massive) stars (Rogers et al. 2012) can induce time-dependent variations in the direction of the stellar surface spin. Given that XO-3 is a fairly hot and fairly massive star, we tested whether this type of stellar polar wander occurs in this system.

The combination of estimates of $V_* \sin i_*$ (from spectroscopic measurements) and V_* (from light-curve measurements) can provide the stellar spin vector of a star along the line of sight (i_*). Although the spectroscopic rotation velocity obtained from Johns-Krull et al. (2008; $V_{*\text{before}} \sin i_{*\text{before}} = 18.54 \pm 0.17 \text{ km s}^{-1}$) agrees with the average of Winn et al. (2009), Hirano et al. (2011), Torres et al. (2012), and Brewer et al. (2016; $V_{*\text{after}} \sin i_{*\text{after}} = 17.9 \pm 0.5 \text{ km s}^{-1}$) within 1.2σ , we cannot constrain the possible variation of the stellar spin vector (Δi_*) that might occur, since XO-3 did not leave a sufficient signal (which would typically manifest as periodic photometric variations from starspots) in its light curve to measure its true rotation velocity (V_*).

However, the difference between the stellar spin vector of XO-3 along the line of sight before Hébrard et al. (2008) and after Winn et al. (2009; $\Delta i_* = i_{*\text{after}} - i_{*\text{before}} = \arcsin\left(\frac{V_{*\text{after}} \sin i_{*\text{after}}}{V_*}\right) - \arcsin\left(\frac{V_{*\text{before}} \sin i_{*\text{before}}}{V_*}\right)$) only depends on the true rotational velocity of the star V_* ; if we assume that the rotational velocity of the star, V_* , does not change over time, this means that the rotational velocity before Hébrard et al. (2008) and after Winn et al. (2009) $V_{*\text{before}} = V_{*\text{after}} = V_*$. The maximum possible variation is then $\Delta i_* = 15^\circ 26 \pm 5^\circ 82$, when $V_* = \max(V_* \sin i_{*\text{before}}, V_* \sin i_{*\text{after}}) = V_{*\text{before}} = 18.54 \pm 0.17 \text{ km s}^{-1}$. This agrees with no change (e.g., $\Delta i_* = 0^\circ$) within 2.6σ . This is the maximum change that is consistent with current data, since here we assume the minimum possible value of V_* corresponds to the largest possible Δi_* .

Orbital Angular Momentum Vector. Precession of nodes due to an additional perturber could also cause the temporal variation of the direction of the orbital angular momentum

Table 7
Comparison of the System Parameters before Hébrard et al. (2008) and after Winn et al. (2009)

Parameter	Units	Before Hébrard et al. (2008)	After Winn et al. (2009)	Agreement (σ)
Stellar Parameters:				
M_*	Mass (M_\odot)	$1.225^{+0.090}_{-0.097}$	$1.216^{+0.087}_{-0.092}$	0.07
R_*	Radius (R_\odot)	1.395 ± 0.060	1.325 ± 0.050	0.9
L_*	Luminosity (L_\odot)	$3.07^{+0.34}_{-0.32}$	$2.81^{+0.29}_{-0.27}$	0.6
ρ_*	Density (cgs)	$0.634^{+0.067}_{-0.059}$	$0.734^{+0.061}_{-0.055}$	1.18
$\log g$	Surface gravity (cgs)	4.236 ± 0.030	4.277 ± 0.024	1.07
T_{eff}	Effective temperature (K)	6467^{+83}_{-81}	6490^{+83}_{-79}	0.2
[Fe/H]	Metallicity	$-0.174^{+0.079}_{-0.078}$	$-0.179^{+0.081}_{-0.082}$	0.04
[Fe/H] ₀	Initial metallicity	$-0.021^{+0.072}_{-0.071}$	-0.041 ± 0.070	0.2
Age	Age (Gyr)	$2.7^{+1.6}_{-1.1}$	$2.2^{+1.6}_{-1.0}$	0.26
EEP	Equal evolutionary point	365^{+38}_{-23}	349^{+38}_{-18}	0.38
A_v	V-band extinction	$0.068^{+0.092}_{-0.048}$	$0.072^{+0.090}_{-0.051}$	0.04
σ_{SED}	SED photometry error scaling	$2.8^{+2.8}_{-1.1}$	$2.6^{+2.5}_{-1.0}$	0.07
d	Distance (pc)	$181.6^{+8.8}_{-9.0}$	$173.4^{+7.6}_{-7.8}$	0.7
π	Parallax (mas)	$5.51^{+0.29}_{-0.25}$	$5.77^{+0.27}_{-0.24}$	0.71
Planetary Parameters:				
P	Period (days)	3.1915219 ± 0.0000035	$3.1915264^{+0.0000020}_{-0.0000019}$	1.12
R_p	Radius (R_J)	$1.229^{+0.055}_{-0.056}$	$1.183^{+0.050}_{-0.049}$	0.62
T_C	Time of transit (BJD _{TDB})	$2454449.86996^{+0.00025}_{-0.00026}$	2454449.8685 ± 0.0016	0.9
T_0	Optimal transit time (BJD _{TDB})	$2454357.31583 \pm 0.00023$	2454858.3839 ± 0.0016	...
a	Semimajor axis (au)	$0.0455^{+0.0011}_{-0.0012}$	$0.0454^{+0.0011}_{-0.0012}$	0.06
i	Inclination (deg)	$84.08^{+0.38}_{-0.40}$	$84.67^{+0.31}_{-0.30}$	1.17
e	Eccentricity	0.261 ± 0.015	$0.2887^{+0.0061}_{-0.0059}$	1.71
ω_*	Argument of periastron (deg)	$-11.9^{+6.3}_{-6.0}$	-15.4 ± 2.3	0.52
T_{eq}	Equilibrium temperature (K)	1727 ± 35	1691 ± 31	0.77
M_p	Mass (M_J)	$11.93^{+0.69}_{-0.71}$	$11.56^{+0.59}_{-0.63}$	0.40
K	RV semiamplitude (m s ⁻¹)	1474 ± 45	1449^{+26}_{-27}	0.48
$\log K$	Log of RV semiamplitude	3.169 ± 0.013	$3.1612^{+0.0077}_{-0.0082}$	0.51
R_p/R_*	Radius of planet in stellar radii	$0.09050^{+0.00052}_{-0.00054}$	$0.09174^{+0.00063}_{-0.00064}$	1.49
a/R_*	Semimajor axis in stellar radii	$7.01^{+0.24}_{-0.23}$	$7.36^{+0.20}_{-0.19}$	1.15
δ	Transit depth (fraction)	$0.008191^{+0.000095}_{-0.000097}$	0.00842 ± 0.00012	1.48
Depth	Flux decrement at midtransit	$0.008191^{+0.000095}_{-0.000097}$	0.00842 ± 0.00012	1.48
τ	Ingress/egress transit duration (days)	$0.01948^{+0.00089}_{-0.00090}$	0.0182 ± 0.0010	0.96
T_{14}	Total transit duration (days)	$0.12298^{+0.00083}_{-0.00085}$	$0.12315^{+0.00094}_{-0.00093}$	0.13
T_{FWHM}	FWHM transit duration (days)	0.10350 ± 0.00046	$0.10495^{+0.00053}_{-0.00054}$	2.07
b	Transit impact parameter	$0.713^{+0.013}_{-0.015}$	$0.679^{+0.019}_{-0.021}$	1.38
b_S	Eclipse impact parameter	$0.640^{+0.039}_{-0.037}$	$0.582^{+0.022}_{-0.023}$	1.28
τ_S	Ingress/egress eclipse duration (days)	$0.0159^{+0.0018}_{-0.0015}$	$0.01404^{+0.00084}_{-0.00080}$	0.94
$T_{S,14}$	Total eclipse duration (days)	$0.1182^{+0.0031}_{-0.0036}$	$0.1142^{+0.0022}_{-0.0023}$	1.04
$T_{S,\text{FWHM}}$	FWHM eclipse duration (days)	$0.1023^{+0.0012}_{-0.0021}$	$0.1001^{+0.0014}_{-0.0016}$	1.1
$\delta_{S,3.6\mu\text{m}}$	Blackbody eclipse depth at 3.6 μm (ppm)	754 ± 38	731^{+36}_{-35}	0.45
$\delta_{S,4.5\mu\text{m}}$	Blackbody eclipse depth at 4.5 μm (ppm)	973 ± 42	951 ± 40	0.38
ρ_p	Density (cgs)			$7.97^{+1.0}_{-0.90}$ $8.64^{+0.93}_{-0.83}$ 0.52
$\log g_p$	Surface gravity	$4.292^{+0.035}_{-0.036}$	$4.310^{+0.029}_{-0.028}$	0.39
Θ	Safronov number	$0.722^{+0.043}_{-0.041}$	$0.730^{+0.034}_{-0.033}$	0.15
$\langle F \rangle$	Incident flux (10 ⁹ erg s ⁻¹ cm ⁻²)	$1.89^{+0.16}_{-0.15}$	$1.71^{+0.13}_{-0.12}$	0.9
T_p	Time of periastron (BJD _{TDB})	$2454449.234^{+0.050}_{-0.051}$	2454449.230 ± 0.016	0.08
T_S	Time of eclipse (BJD _{TDB})	$2454448.785^{+0.026}_{-0.028}$	$2454448.8326^{+0.0074}_{-0.0078}$	1.64
T_A	Time of ascending node (BJD _{TDB})	$2454449.293^{+0.021}_{-0.023}$	$2454449.3025^{+0.0066}_{-0.0067}$	0.40
T_D	Time of descending node (BJD _{TDB})	$2454447.809^{+0.045}_{-0.046}$	$2454447.869^{+0.021}_{-0.020}$	1.19
$e \cos \omega_*$...	$0.254^{+0.013}_{-0.014}$	$0.2784^{+0.0038}_{-0.0041}$	1.68
$e \sin \omega_*$...	-0.053 ± 0.029	-0.077 ± 0.012	0.76
$M_p \sin i$	Minimum mass (M_J)	$11.87^{+0.68}_{-0.71}$	$11.51^{+0.59}_{-0.62}$	0.39
M_p/M_*	Mass ratio	$0.00932^{+0.00038}_{-0.00036}$	$0.00909^{+0.00029}_{-0.00027}$	0.49
d/R_*	Separation at midtransit	$6.90^{+0.40}_{-0.38}$	$7.31^{+0.24}_{-0.23}$	0.91
P_T	A priori nongrazing transit prob	$0.1317^{+0.0077}_{-0.0073}$	0.1243 ± 0.0039	0.86
$P_{T,G}$	A priori transit prob	$0.1579^{+0.0093}_{-0.0088}$	$0.1494^{+0.0049}_{-0.0048}$	0.81
P_S	A priori nongrazing eclipse prob	$0.1466^{+0.0033}_{-0.0034}$	$0.1450^{+0.0034}_{-0.0035}$	0.33

Table 7
(Continued)

Parameter	Units	Before Hébrard et al. (2008)	After Winn et al. (2009)	Agreement (σ)
$P_{S,G}$	A priori eclipse prob	0.1758 ± 0.0041	$0.1743^{+0.0043}_{-0.0044}$	0.25
Wavelength Parameters:				
u_{1B}	Linear limb-darkening coeff	0.500 ± 0.032	0.488 ± 0.050	0.2
u_{2B}	Quadratic limb-darkening coeff	0.277 ± 0.030	0.277 ± 0.050	0.0
u_{1I}	Linear limb-darkening coeff	0.190 ± 0.018	0.221 ± 0.042	0.68
u_{2I}	Quadratic limb-darkening coeff	$0.299^{+0.017}_{-0.018}$	0.300 ± 0.044	0.02
u_{1R}	Linear limb-darkening coeff	$0.272^{+0.019}_{-0.020}$	0.258 ± 0.016	0.56
u_{2R}	Quadratic limb-darkening coeff	0.324 ± 0.018	0.319 ± 0.015	0.21
$u_{1Sloanz}$	Linear limb-darkening coeff	0.166 ± 0.021
$u_{2Sloanz}$	Quadratic limb-darkening coeff	0.294 ± 0.021
$u_{1Sloani}$	Linear limb-darkening coeff	...	0.306 ± 0.044	...
$u_{2Sloani}$	Quadratic limb-darkening coeff	...	0.340 ± 0.045	...
u_{1V}	Linear limb-darkening coeff	0.364 ± 0.023	$0.341^{+0.049}_{-0.050}$	0.42
u_{2V}	Quadratic limb-darkening coeff	$0.324^{+0.022}_{-0.021}$	0.310 ± 0.049	0.26

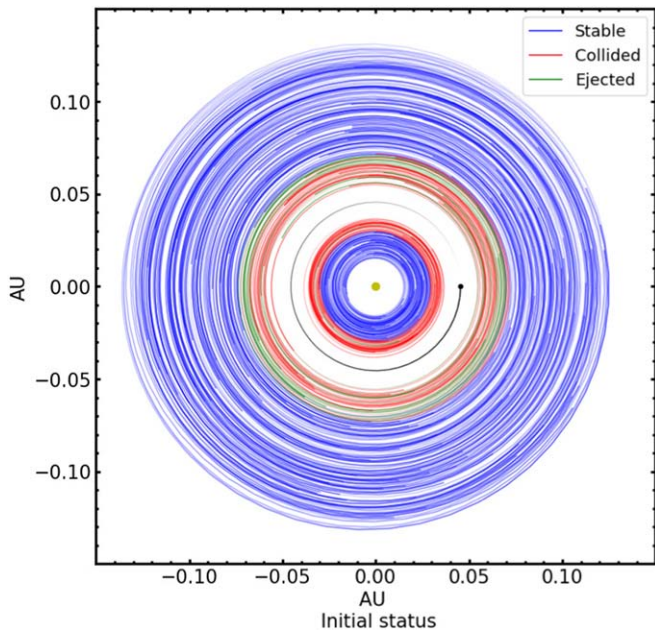


Figure 5. A top-down view of the XO-3 system. Initial orbits of 300 test particles are evenly distributed over 1.3–7.5 mutual Hill radii with XO-3b. Orbits remaining after a 10^6 yr integration are shown in blue. All orbits lying within 3.5 mutual Hill radii of XO-3b have been destabilized. Among the unstable particles, 80% collide with XO-3 (red), and, as a consequence of XO-3b’s large mass, 20% are ejected (green).

vector (Innanen et al. 1997). Precession can manifest as temporal variation of the transit profile, with evolution occurring in the impact parameter (b), the transit inclinations (i), the transit duration (T_{14}), and the transit depth (δ). We thus separately fit the transit and radial-velocity data before the R-M measurement conducted by Hébrard et al. (2008), and after the R-M measurement conducted by Winn et al. (2009). As shown in Table 7 and Figure 6, we found that the transit inclinations derived from the data before Hébrard et al. (2008) and after Winn et al. (2009) are in excellent agreement with each other with only $\Delta i = 0^\circ.59 \pm 0^\circ.5$ difference, which means that the orbital angular momentum vector of XO-3b along the line of sight agrees with no change within 1.2σ .

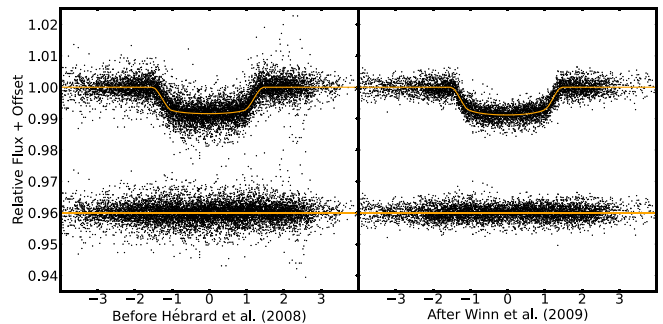


Figure 6. Left: phased transit light curves before the R-M measurement conducted by Hébrard et al. (2008). Right: phased transit light curves after the R-M measurement conducted by Winn et al. (2009). The best-fitting model for each data set is overlotted as a solid orange line. The two transit profiles are in good agreement.

In conclusion, we found no evidence for temporal changes of either the stellar spin vector or the orbital angular momentum vector of XO-3b along the line of sight.

Systematic Noise. Winn et al. (2009) and Hirano et al. (2011) suspected that the discrepancy in multiple R-M measurements for XO-3b is most likely due to systematic errors in the data sets (Hébrard et al. 2008), which will lead to underestimated uncertainties in λ .

We bin the residuals of each of three R-M measurements (Hébrard et al. 2008; Winn et al. 2009; Hirano et al. 2011) into bin sizes $N = 1 - 15$ and evaluate the rms of the data. We found that the rms of the time-binned residuals for all three data sets decreases more slowly than $N^{1/2}$ ($N^{1/3}$ for Hébrard et al. 2008; $N^{1/5}$ for Winn et al. 2009; $N^{1/3}$ for Hirano et al. 2011), suggesting that strong correlated noise is present.

This is also clear in the residual panels of Figure 7. In this figure, we took the data directly from Hébrard et al. (2008), Winn et al. (2009), and Hirano et al. (2011), and we subtracted away the baseline RV trend from each data set using the parameters reported by each respective paper. We then plotted the reported model (using the previous authors’ results) in Figure 7, showing the residual amplitudes below.

The data from all three data sets (Hébrard et al. 2008; Winn et al. 2009; Hirano et al. 2011) suffer from strong systematic errors: that is, the residuals show clear structure that remains

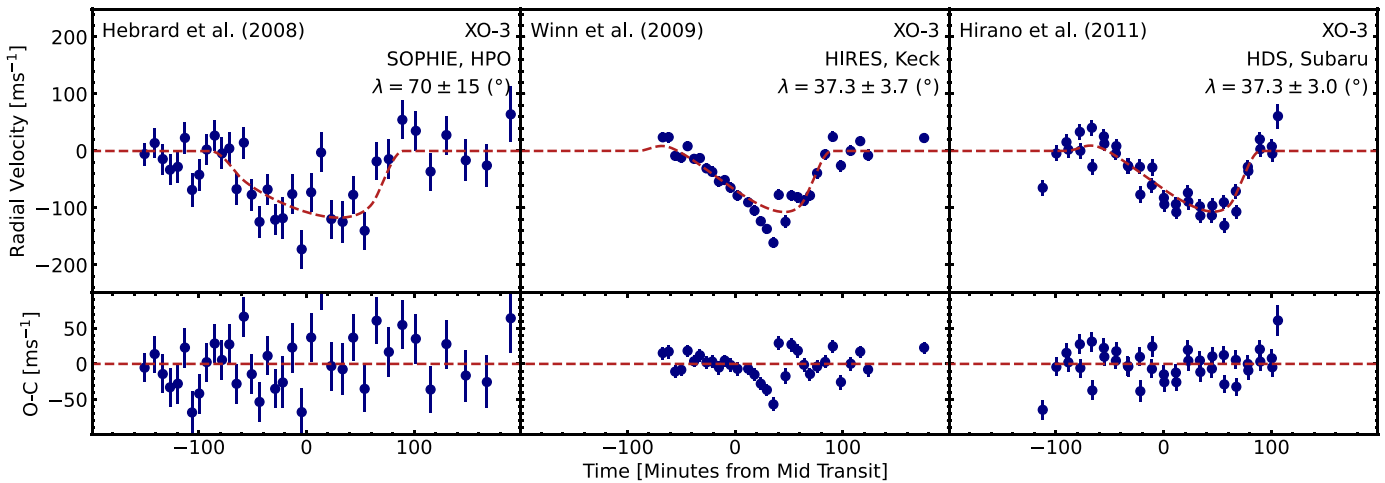


Figure 7. Spectroscopic radial velocities of XO-3 from Hébrard et al. (2008; left), Winn et al. (2009; center), and Hirano et al. (2011; right) as a function of orbital phase (minutes from midtransit), coupled with the best-fitting R-M models (red dashed line). The rms of the residuals from the three works, from left to right, is 40, 18, and 23 m s^{-1} .

after the best-fitting model has been subtracted from the data. This is not surprising for a hot and massive star like XO-3, and it leads to an underestimate of uncertainties in λ .

Although current observations still allow for quite a bit of temporal variation of the spin-orbit angle of XO-3 system, we have demonstrated that the disagreement between sky-projected spin-orbit angles measured from previous studies very likely results from the underestimate of the uncertainties of λ due to the presence of systematic noise in the data, with no requirement for a true temporal variation in the spin-orbit angle. We also find no strong evidence that the two other angles have changed.

The origin and evolution of spin-orbit misalignments remains one of the most interesting unsolved problems posed by the observed properties of the exoplanets (Winn & Fabrycky 2015; Albrecht et al. 2021). A definitive assessment would be easier to formulate if measurements of spin-orbit angles could be made for a variety of system types. The R-M effect, however, is much more easily measured when transits are frequent and deep. Therefore, while R-M observations of small planets and/or long-period planets play a critical role in understanding the origin of spin-orbit misalignment (Albrecht et al. 2013; Zhou et al. 2018; Wang et al. 2018b, 2021, 2022; Rice et al. 2021), they are difficult to successfully carry out.

Although the R-M effect was first established through the observation of an eclipsing binary more than a century ago (Schlesinger 1910), such measurements of low-mass eclipsing binaries are surprisingly rare (see BANANA Project; Albrecht et al. 2007). NASA’s TESS mission has been steadily discovering suitable targets (e.g., Huang et al. 2018; Cañas et al. 2019; Günther et al. 2019; Jones et al. 2019; Wang et al. 2019) and will detect a large number of low-mass eclipsing binaries orbiting bright stars that are suitable for R-M follow-up. This new population may shed light on not only planet formation, but also on the genesis of low-mass stars.

K.W. thanks Yale College for supporting this work through the First-Year Research Fellowship in the Sciences and the Edward A Bouchet Fellowship. S.W. thanks the Heising-Simons Foundation for their generous support. J.A.B. thanks MIT’s Kavli Institute for its support. M.R. is supported by the

National Science Foundation Graduate Research Fellowship Program under grant No. DGE-1752134. This work is supported by Astronomical Big Data Joint Research Center, co-funded by National Astronomical Observatories, Chinese Academy of Sciences and Alibaba Cloud. The research was carried out in part at the Jet Propulsion Laboratory, California Institute of Technology, under a contract with the National Aeronautics and Space Administration (80NM0018D0004). We thank Jason Eastman, John Michael Brewer, and Pia Cortes-Zuleta for useful discussions.

ORCID iDs

Songhu Wang <https://orcid.org/0000-0002-7846-6981>
 Jennifer Burt <https://orcid.org/0000-0002-0040-6815>
 Malena Rice <https://orcid.org/0000-0002-7670-670X>
 Xian-Yu Wang <https://orcid.org/0000-0002-0376-6365>
 Yong-Hao Wang <https://orcid.org/0000-0003-0261-6362>
 Steven S. Vogt <https://orcid.org/0000-0001-7177-7456>
 R. Paul Butler <https://orcid.org/0000-0003-1305-3761>
 Brett Addison <https://orcid.org/0000-0003-3216-0626>
 Brad Holden <https://orcid.org/0000-0002-6153-3076>
 Zhen-Yu Wu <https://orcid.org/0000-0001-8037-1984>
 Hui-Gen Liu <https://orcid.org/0000-0001-5162-1753>
 Hui Zhang <https://orcid.org/0000-0003-3491-6394>
 Ji-Lin Zhou <https://orcid.org/0000-0003-1680-2940>
 Gregory Laughlin <https://orcid.org/0000-0002-3253-2621>

References

- Albrecht, S., Reffert, S., Snellen, I., Quirrenbach, A., & Mitchell, D. S. 2007, *A&A*, 474, 565
 Albrecht, S., Marcussen, M. L., Winn, J. N., Dawson, R. I., & Knudstrup, E. 2021, *ApJL*, 916, L1
 Albrecht, S., Winn, J. N., Marcy, G. W., et al. 2013, *ApJ*, 771, 11
 Baranne, A., Queloz, D., Mayor, M., et al. 1996, *A&AS*, 119, 373
 Bate, M. R., Lodato, G., & Pringle, J. E. 2010, *MNRAS*, 401, 1505
 Batygin, K. 2012, *Natur*, 491, 418
 Batygin, K., Bodenheimer, P. H., & Laughlin, G. P. 2016, *ApJ*, 829, 114
 Beatty, T. G., & Gaudi, B. S. 2015, *PASP*, 127, 1240
 Bertin, E., & Arnouts, S. 1996, *A&AS*, 117, 393
 Bodenheimer, P., Hubickyj, O., & Lissauer, J. J. 2000, *Icar*, 143, 2
 Bonomo, A. S., Desidera, S., Benatti, S., et al. 2017, *A&A*, 602, A107
 Bouchy, F., Bonomo, A. S., Santerne, A., et al. 2011, *A&A*, 533, A83

- Brewer, J. M., Fischer, D. A., Valenti, J. A., & Piskunov, N. 2016, *ApJS*, **225**, 32
- Burt, J., Feng, F., Holden, B., et al. 2021, *AJ*, **161**, 10
- Burt, J., Holden, B., Hanson, R., et al. 2015, *JATIS*, **1**, 044003
- Burt, J., Vogt, S. S., Butler, R. P., et al. 2014, *ApJ*, **789**, 114
- Butler, R. P., Marcy, G. W., Williams, E., et al. 1996, *PASP*, **108**, 500
- Cañas, C. I., Stefánsson, G., Monson, A. J., et al. 2019, *ApJ*, **877**, 29
- Casey, A. R., Hogg, D. W., Ness, M., et al. 2016, arXiv:1603.03040
- Chambers, J. E., Wetherill, G. W., & Boss, A. P. 1996, *Icar*, **119**, 261
- Choi, J., Dotter, A., Conroy, C., et al. 2016, *ApJ*, **823**, 102
- Christiansen, J. L., Vanderburg, A., Burt, J., et al. 2017, *AJ*, **154**, 122
- Claret, A., & Bloemen, S. 2011, *A&A*, **529**, 75
- Cosentino, R., Lovis, C., Pepe, F., et al. 2012, *Proc. SPIE*, **8446**, 84461V
- Cosentino, R., Lovis, C., Pepe, F., et al. 2014, *Proc. SPIE*, **9147**, 91478C
- Crane, J. D., Shectman, S. A., Butler, R. P., et al. 2010, *Proc. SPIE*, **7735**, 773553
- Dawson, R. I. 2014, *ApJL*, **790**, L31
- Dotter, A. 2016, *ApJS*, **222**, 8
- Eastman, J. 2017, EXOFASTv2: Generalized publication-quality exoplanet modeling code, Astrophysics Source Code Library, ascl:1710.003
- Eastman, J., Gaudi, B. S., & Agol, E. 2013, *PASP*, **125**, 83
- Eastman, J., Siverd, R., & Gaudi, B. S. 2010, *PASP*, **122**, 935
- Eversberg, T. 2016, *PASP*, **128**, 115001
- Fabrycky, D., & Tremaine, S. 2007, *ApJ*, **669**, 1298
- Fielding, D. B., McKee, C. F., Socrates, A., Cunningham, A. J., & Klein, R. I. 2015, *MNRAS*, **450**, 3306
- Fulton, B. J., Weiss, L. M., Sinukoff, E., et al. 2015, *ApJ*, **805**, 175
- Garai, Z., Pribulla, T., Hambálek, L., et al. 2017, *AN*, **338**, 35
- Gladman, B. 1993, *Icar*, **106**, 247
- Gomes, R., Deienno, R., & Morbidelli, A. 2017, *AJ*, **153**, 27
- Günther, M. N., Pozuelos, F. J., Dittmann, J. A., et al. 2019, *NatAs*, **3**, 1099
- Hébrard, G., Bouchy, F., Pont, F., et al. 2008, *A&A*, **488**, 763
- Hirano, T., Narita, N., Sato, B., et al. 2011, *PASJ*, **63**, L57
- Huang, C. X., Burt, J., Vanderburg, A., et al. 2018, *ApJL*, **868**, L39
- Innanen, K. A., Zheng, J. Q., Mikkola, S., & Valtonen, M. J. 1997, *AJ*, **113**, 1915
- Johns-Krull, C. M., McCullough, P. R., Burke, C. J., et al. 2008, *ApJ*, **677**, 657
- Jones, M. I., Brahm, R., Espinoza, N., et al. 2019, *A&A*, **625**, A16
- Knutson, H. A., Fulton, B. J., Montet, B. T., et al. 2014, *ApJ*, **785**, 126
- Lai, D. 2016, *AJ*, **152**, 215
- Lai, D., Foucart, F., & Lin, D. N. C. 2011, *MNRAS*, **412**, 2790
- Li, G., Naoz, S., Valsecchi, F., Johnson, J. A., & Rasio, F. A. 2014, *ApJ*, **794**, 131
- Li, G., & Winn, J. N. 2016, *ApJ*, **818**, 5
- Lin, D. N. C., Bodenheimer, P., & Richardson, D. C. 1996, *Natur*, **380**, 606
- Marcy, G. W., & Butler, R. P. 2000, *PASP*, **112**, 137
- McLaughlin, D. B. 1924, *ApJ*, **60**, 22
- Nagasawa, M., Ida, S., & Bessho, T. 2008, *ApJ*, **678**, 498
- Naoz, S. 2016, *ARA&A*, **54**, 441
- Ness, M., Hogg, D. W., Rix, H.-W., Ho, A. Y., & Zasowski, G. 2015, *AJ*, **619**, 570
- Noguchi, K., Aoki, W., Kawanomoto, S., et al. 2002, *PASJ*, **54**, 855
- Pepe, F., Mayor, M., Rupprecht, G., et al. 2002, *Msngr*, **110**, 9
- Perruchot, S., Kohler, D., Bouchy, F., et al. 2008, *Proc. SPIE*, **7014**, 70140J
- Petrovich, C. 2015, *ApJ*, **805**, 75
- Queloz, D., Eggenberger, A., Mayor, M., et al. 2000, *A&A*, **359**, L13
- Rasio, F. A., & Ford, E. B. 1996, *Sci*, **274**, 954
- Rice, M., & Brewer, J. M. 2020, *ApJ*, **898**, 119
- Rice, M., Wang, S., Howard, A. W., et al. 2021, *AJ*, **162**, 182
- Rogers, T. M., Lin, D. N. C., & Lau, H. H. B. 2012, *ApJL*, **758**, L6
- Rossiter, R. A. 1924, *ApJ*, **60**, 15
- Safronov, V. S. 1972, Evolution of the Protoplanetary Cloud and Formation of the Earth and Planets (Jerusalem: Keter Publishing House)
- Schlesinger, F. 1910, *PAIO*, **1**, 123
- Southworth, J. 2008, *MNRAS*, **386**, 1644
- Southworth, J., Hinse, T. C., Jørgensen, U. G., et al. 2009, *MNRAS*, **396**, 1023
- Southworth, J., Mancini, L., Madhusudhan, N., et al. 2017, *AJ*, **153**, 191
- Spalding, C., & Batygin, K. 2014, *ApJ*, **790**, 42
- Storch, N. I., Anderson, K. R., & Lai, D. 2014, *Sci*, **345**, 1317
- ter Braak, C. J. F. 2006, *Stat. Comput.*, **16**, 239
- Torres, G., Fischer, D. A., Sozzetti, A., et al. 2012, *ApJ*, **757**, 161
- Tull, R. G. 1998, *Proc. SPIE*, **3355**, 387
- Tull, R. G., MacQueen, P. J., Sneden, C., & Lambert, D. L. 1995, *PASP*, **107**, 251
- Valenti, J. A., & Fischer, D. A. 2005, *ApJS*, **159**, 141
- Valenti, J. A., & Piskunov, N. 1996, *A&AS*, **118**, 595
- Vogt, S. S., Allen, S. L., Bigelow, B. C., et al. 1994, *Proc. SPIE*, **2198**, 362
- Vogt, S. S., Burt, J., Meschiari, S., et al. 2015, *ApJ*, **814**, 12
- Vogt, S. S., Radovan, M., Kibrick, R., et al. 2014, *PASP*, **126**, 359
- Wang, S., Addison, B., Fischer, D. A., et al. 2018b, *AJ*, **155**, 70
- Wang, S., Jones, M., Shporer, A., et al. 2019, *AJ*, **157**, 51
- Wang, S., Wang, X.-Y., Wang, Y.-H., et al. 2018c, *AJ*, **156**, 181
- Wang, S., Winn, J. N., Addison, B. C., et al. 2021, *AJ*, **162**, 50
- Wang, S., Wu, D.-H., Addison, B. C., et al. 2018a, *AJ*, **155**, 73
- Wang, X.-Y., Rice, M., Wang, S., et al. 2022, *ApJS*, **926**, L8
- Wang, X.-Y., Wang, S., Hinse, T. C., et al. 2018, *PASP*, **130**, 064401
- Wang, X.-Y., Wang, Y.-H., Wang, S., et al. 2021a, *ApJS*, **255**, 15
- Wang, Y.-H., Wang, S., Hinse, T. C., et al. 2019, *AJ*, **157**, 82
- Wang, Y.-H., Wang, S., Liu, H.-G., et al. 2017, *AJ*, **154**, 49
- Winn, J. N., Fabrycky, D., Albrecht, S., & Johnson, J. A. 2010, *ApJL*, **718**, L145
- Winn, J. N., & Fabrycky, D. C. 2015, *ARA&A*, **53**, 409
- Winn, J. N., Holman, M. J., Torres, G., et al. 2008, *ApJ*, **683**, 1076
- Winn, J. N., Johnson, J. A., Fabrycky, D., et al. 2009, *ApJ*, **700**, 302
- Wong, I., Knutson, H. A., Cowan, N. B., et al. 2014, *ApJ*, **794**, 134
- Wu, Y., & Lithwick, Y. 2011, *ApJ*, **735**, 109
- Wu, Y., Murray, N. W., & Ramsahai, J. M. 2007, *ApJ*, **670**, 820
- Zhou, G., Rodriguez, J. E., Vanderburg, A., et al. 2018, *AJ*, **156**, 93
- Zhou, X., Chen, J., Xu, W., et al. 1999, *PASP*, **111**, 909
- Zhou, X., Jiang, Z.-J., Xue, S.-J., et al. 2001, *CJAA*, **1**, 372